Quantum size effects in metal nanofilms: Comparison of an electron-gas model and density functional theory calculations

Yong Han[1,*] and Da-Jiang Liu[2]
[1]*Institute of Physical Research and Technology, Iowa State University, Ames, Iowa 50011, USA*
[2]*Ames Laboratory, U.S. DOE, Iowa State University, Ames, Iowa 50011, USA*
(Received 19 June 2009; revised manuscript received 21 August 2009; published 2 October 2009)

Effects of quantum confinement of electrons in metal nanofilms are analyzed using a noninteracting electron-gas model. Electrons are confined within a potential well with infinite-height barrier. The positions of the barrier are at a fixed distance away from the geometric boundaries of the film such that the surface-charge neutrality requirement is maintained at the bulk limit. The model predicts oscillations in basic physical properties such as the Fermi energy, electron density, surface free energy, and dipole layer moment as a function of film thickness. We compare predictions of this electron-gas model with first-principles density functional theory (DFT) for ten metal films. For Ag(110), Ag(100), Mg(0001), Al(111), Al(110), and Pb(111) films, the oscillation features obtained from the model are in good quantitative agreement with those from DFT calculations. However, for Al(100), Pb(110), and Pb(100) films, oscillation behavior in the model differs from DFT calculations. For Ag(111), the electron-gas model predicts weak oscillations, in contrast to the DFT calculations, in which no noticeable regular oscillations are observed.

DOI: 10.1103/PhysRevB.80.155404 PACS number(s): 68.55.jd, 71.10.Ca, 73.61.At, 71.15.Nc

I. INTRODUCTION

Development of nanotechnologies involving deposition of metals on substrates could benefit from further theoretical analysis and understanding of the electronic-structure effects associated with nanocluster and nanofilm geometries. If the size of the nanostructure is comparable to the corresponding electron Fermi wavelength, various physical properties may exhibit strong size dependence due to effects of quantum confinement of electrons.[1–10] This phenomenon is usually called the quantum-size effect (QSE). For metal nanofilms, many physical quantities, such as thermodynamic stability,[11–13] electrical resistivity,[14] superconducting critical temperature,[15] the perpendicular upper critical field,[16] surface adhesion,[17] thermal-expansion coefficient,[18] surface free energy,[19,20] surface diffusion barriers,[20–22] surface adsorption energy,[20,23] work function,[24,25] etc., oscillate as a function of film thickness. Because of the possibility of significant differences between the properties of a metal nanostructure and its bulk counterpart, the measurement and interpretation of such properties for the former has received considerable theoretical and experimental interest.

QSE in metal nanofilms was investigated by Schulte[26] within the framework of a jellium model which generally includes interactions between electrons. It became immediately obvious that much of the oscillatory feature has its origin in the discreteness of the energy levels due to confinement of electrons with the finite width of the film and a noninteracting electron-gas model can capture most of the features as shown by Schulte in the same paper. Surprisingly, despite its simplicity, there are still some controversies regarding the usefulness of the electron-gas model in describing QSE.[27,28] As a benchmark, in this paper, we study the QSE in freestanding metal thin films using a free-electron-gas model with infinite-height barrier. We find that the results are very sensitive to the choice of the boundary position of potential well relative to the geometric surface of the system, mimicking the spilling of electrons outside the thin films in real systems. By judiciously choosing this separation, we find that very good agreement with the jellium model can be achieved using the infinite barrier model.

On the other hand, density functional theory (DFT) calculations including the crystal structure of real physical systems can result in significantly different QSE behavior from the jellium model or the electron-gas model. In this paper, we study the following nanofilms: Ag(111), Ag(110), Ag(100), Mg(0001), Al(111), Al(110), Al(100), Pb(111), Pb(110), and Pb(100), using DFT. These choices are representative of systems with different valance electrons (from 1 to 4), different crystal structures (fcc and hcp), and different surfaces indices. We find different degrees of agreement between DFT and electron-gas model predictions for QSE in these systems.

In Sec. II, we will present a detailed analysis (including Fermi energy level, ground-state electron density, and surface free energy) of the electron-gas model (EGM) for metal nanofilms. In Sec. III, we apply these results to ten typical metal systems and also compare against the results from DFT calculations. In Sec. IV, we discuss the limitations of the EGM and we provide a summary and conclusions in Sec. V. Other results, including the energy per electron and the dipole layer moment from the EGM, are given in Appendices A and B.

II. THE ELECTRON-GAS MODEL

In this section, we use a model of noninteracting electrons in a square-well potential well with infinite-height barrier as the simplest model for QSE due to the confinement of electrons within a metal thin film. Similar studies were already performed by Pitarke and Eguiluz,[27] and more recently by Wu and Zhang.[28] However, due to different choices of the hard-wall boundary conditions in accounting for the spilling of electrons into the vacuum, very different results were ob-

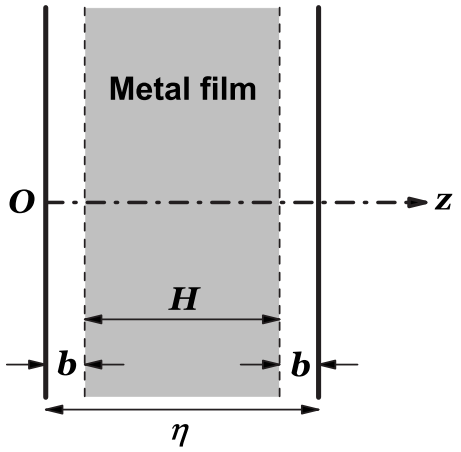

FIG. 1. Schematic illustration of a metal electron-gas nanofilm in a square-well potential with the surface charge-neutrality requirement. Two vertical dashed lines represent the geometrical surfaces of the metal film while two vertical thick solid lines represent the potential boundaries.

tained. Here, we show that a very simple treatment of the spilling effect, choosing the hard wall at a fixed distance from geometric surface of the thin film, provides very satisfactory agreement with the fully self-consistent jellium model.

As in the jellium model, we assume that the positive charge is uniformly distributed within the thin film. However, we emphasize that for most quantities, the distribution of the positive charge is inconsequential for the free-electron-gas model. The boundaries of the potential well are at a distance b from the jellium edge (corresponding to the geometric surface of the film) as shown in Fig. 1. Thus, the effective potential simplified by an infinite barrier, i.e., the hard-wall potential, is expressed as

$$V_{\text{eff}} = \begin{cases} 0 & \text{for } 0 < z < \eta \\ \infty & \text{for } z < 0, z > \eta \end{cases}, \tag{1}$$

where $\eta \equiv H + 2b$ is the thickness of potential well and H is the geometric thickness of the film.

As early as 1936, Bardeen[29] showed that for a semi-infinite surface, the requirement of charge neutrality imposes a dependency on the position of the square-well potential boundary and the corresponding barrier height U_0 in a free-electron-gas model for a metal surface. For $U_0 \to \infty$ (i.e., the hard-wall potential), the separation, b, satisfies

$$b = \frac{3\pi}{8k_F} = \frac{3}{16}\lambda_F, \tag{2}$$

where k_F and λ_F are the Fermi wave vector and Fermi wavelength for a bulk metal in the standard free-electron-gas model, i.e., the Drude-Sommerfeld model,[30] respectively. The values of k_F and λ_F for five metals are listed in Table I. For a finite U_0, if b is set to zero, then the surface-charge neutrality requires that U_0 must equal the bulk-metal Fermi energy E_F. Ignoring the relationship of b and U_0 can lead to a deviation of a factor of 5 in the estimate of the bulk surface free energy. However, only a 10% variation is found for the complete range of possible values for b and U_0 by satisfying

TABLE I. Structures, zero-temperature geometrical constants, and corresponding calculated Drude-Sommerfeld model parameters for bulk metal Ag, Au, Mg, Al, and Pb crystals. All experimental lattice constants are the extrapolated values from nonzero temperatures. For Ag and Al, see Ref. 31; for Au, see Ref. 32; for Pb, see Ref. 33; for Mg, we obtain the zero-temperature lattice constants a and c from a second-order polynomial extrapolation by using the data collected by Pearson.[34] All DFT lattice constants are from this work. All interlayer spacings and calculated model parameters correspond to their corresponding experimental lattice constants.

	Ag	Au	Mg	Al	Pb
Valence electron number Z	1	1	2	3	4
Crystalline structure	fcc	fcc	hcp	fcc	fcc
Experimental lattice constants (Å)	a=4.0690	a=4.0650	a=3.1916 c=5.1815	a=4.0317	a=4.9150
DFT lattice constants (Å)	a=4.166	a=4.168	a=3.191 c=5.195	a=4.049	a=5.035
(111) interlayer spacing $a/\sqrt{3}$ (Å)	2.3492	2.3469		2.3277	2.8377
(0001) interlayer spacing $c/2$ (Å)			2.5908		
(110) interlayer spacing $\sqrt{2}a/4$ (Å)	1.4386	1.4372		1.4254	1.7377
(100) interlayer spacing $a/2$ (Å)	2.0345	2.0325		2.0159	2.4575
Positive charge density p (Å^{-3})	0.059374	0.059550	0.043755	0.061037	0.033689
Wigner-Seitz radius r_s (Å)	1.5902	1.5886	1.3973	1.0924	1.2100
Fermi wavevector k_F (Å^{-1})	1.2069	1.2081	1.3735	1.7568	1.5861
Fermi wavelength λ_F (Å)	5.2060	5.2009	4.5746	3.5766	3.9615
Fermi energy E_F (eV)	5.54968	5.56061	7.18745	11.75839	9.58451
Energy per atom σ_{bulk} (eV)	3.32981	3.33637	4.31247	7.05504	5.75070

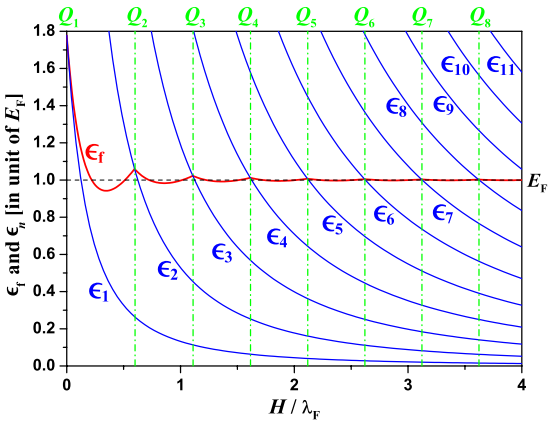

FIG. 2. (Color online) Fermi energy ϵ_f (red solid curve) from Eq. (8) and eigenvalues $\epsilon_{n=1,2,3,\ldots}$ (blue solid curves) from Eq. (5) versus nanofilm thickness H. Black dashed line corresponds to the bulk Fermi energy E_F and green dash-dotted vertical lines represent the cusp positions Q_n from Eq. (10).

the charge-neutrality requirement.[35] Thus, in this paper, we restrict our attention to the case of $U_0 \to \infty$.

For a metal nanofilm with the thickness H, if one does not allow for any charge spilling by simply setting b to zero, then a spurious term $\propto 1/H$ appears in the expression of Fermi wave vector of the metal nanofilm.[36–39] When this type of electron-gas model without charge spilling[28,40] is used to calculate electronic properties of a metal nanofilm, there is a significant discrepancy between the results from the EGM and DFT calculations, as will be discussed below.

For a metal nanofilm with the finite thickness H, in principle, the parameter b (at the limit of $U_0 \to \infty$) can also depend on H. However, if one assumes that the highest-occupied energy level ϵ_f (defined as the Fermi energy of the film) is also H dependent, the charge neutrality requirement only imposes a relation between ϵ_f and b. In Pitarke and Eguiluz's work,[27] ϵ_f is fixed at the bulk value, and b is adjusted. In Wu and Zhang's work,[28] b is set to zero while ϵ_f is adjusted. In this paper, we fix b at the bulk film value $\frac{3}{16}\lambda_F$ and adjust ϵ_f with varying H.

Solving the corresponding Schrödinger equation for a periodic $D \times D$ slab (supercell) along xy plane of the nanofilm, one can obtain the single-electron wave functions as

TABLE II. Cusp position H_n and the difference $H_{n+1}-H_n$ between two nearest-neighboring cusps in Fig. 2. H_n is in units of λ_F.

n	H_n	$H_{n+1}-H_n$
1	0.000000	0.596270
2	0.596270	0.511856
3	1.108125	0.504893
4	1.613018	0.502686
5	2.115704	0.501700
6	2.617404	0.501173
7	3.118578	0.500859
8	3.619436	0.500656

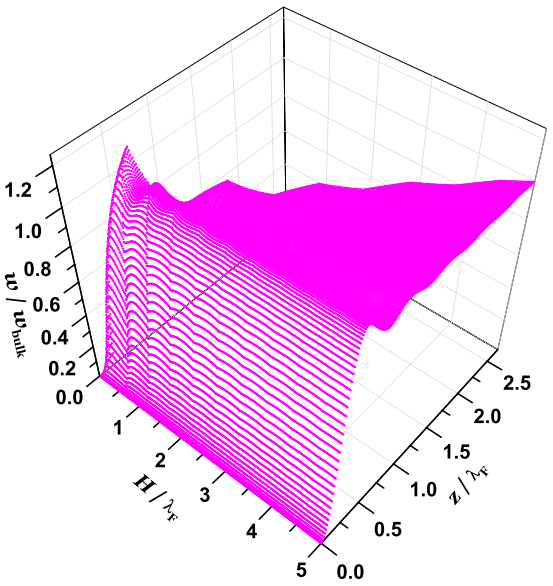

FIG. 3. (Color online) Ground-state electron-density distribution $w(z)$ versus nanofilm thickness H from Eq. (14) and depth z in the range from 0 to $\eta/2$, where $\eta=H+2b$ is the potential-well thickness. $w(z)$ from η to $\eta/2$ is determined from the range above and not shown in the figure.

$$\psi_{k_x,k_y,l}(x,y,z) = \frac{1}{D} e^{i(k_x x + k_y y)} \phi_l(z), \tag{3}$$

where $l=1,2,3,\ldots$ and $k_{x(y)}=2\pi l_{x(y)}/D$ with $l_{x(y)}=0, \pm 1, \pm 2, \ldots$. The so-called quantum well state (QWS) wave functions $\phi_l(z)$ in Eq. (3) are simply

$$\phi_l(z) = \sqrt{\frac{2}{\eta}} \sin\frac{l\pi z}{\eta} \tag{4}$$

and the eigenenergies are

$$\epsilon_l = \frac{\hbar^2}{2m_e}\frac{l^2\pi^2}{\eta^2}, \quad l = 1,2,3,\ldots, \tag{5}$$

where m_e is the mass of an electron. In $\mathbf{k}$ space, the occupied subbands compose a series of Fermi discs defined by[26]

$$\frac{\hbar^2}{2m_e}(k_x^2 + k_y^2) \le \epsilon_f - \epsilon_l, \quad l = 1,2,\ldots,n, \tag{6}$$

where $k_{x(y)}$ is the $x(y)$ component of $\mathbf{k}$ and the Fermi energy ϵ_f is defined as the highest-occupied energy level, which corresponds to the radius of the Fermi sphere. It follows that the maximum number n of Fermi discs can be determined by $\epsilon_n \le \epsilon_f < \epsilon_{n+1}$. Accounting for this feature, one can obtain analytical expressions for various physical properties as a function of film thickness, as discussed separately below.

A. Fermi energy level

Considering the Fermi discs defined by Eqs. (6) and (5), and considering the bulk average electron density, i.e., the Drude-Sommerfeld electron density

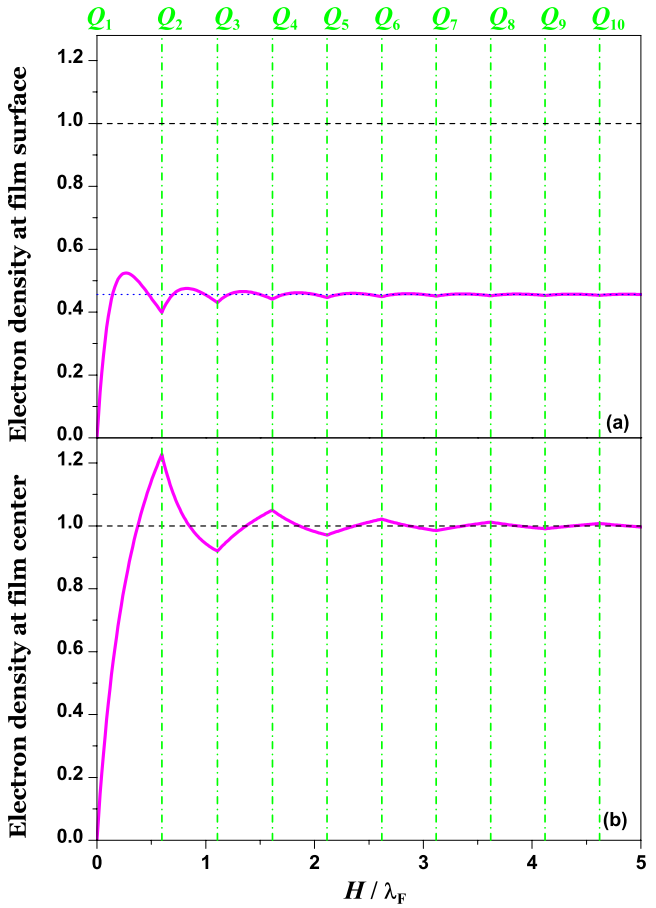

FIG. 4. (Color online) Electron densities (in unit of bulk electron density w_{bulk}) (a) $w(b)$ at the surface and (b) $w(\eta/2)$ at the center of the film, versus nanofilm thickness H from Eq. (14). Green dash-dotted vertical lines represent the cusp positions Q_n from Eq. (10). Dashed black horizontal line corresponds to w_{bulk}. The dotted blue horizontal line in (a) denotes the constant $\kappa = 0.4557\ldots$.

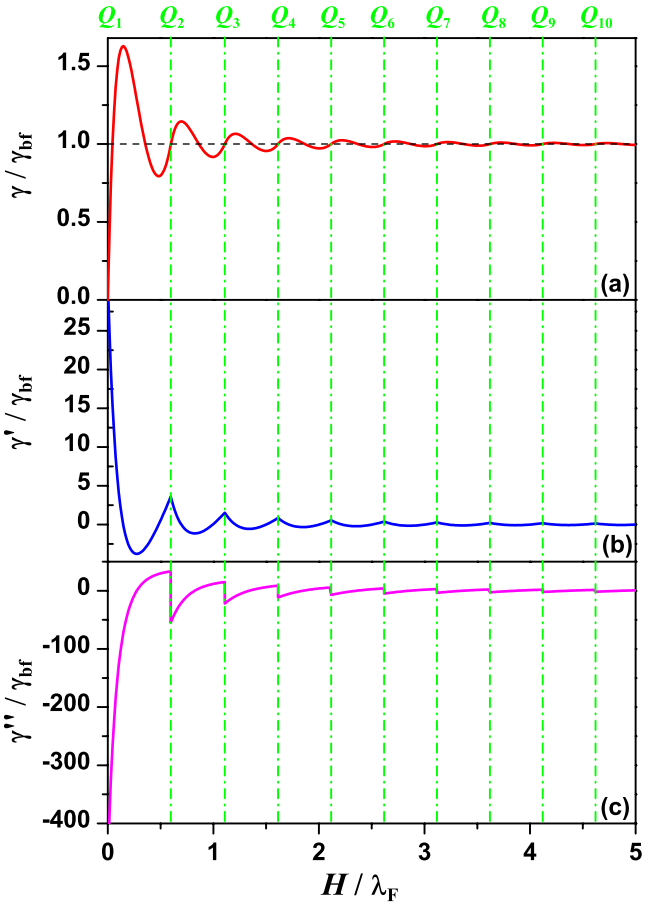

FIG. 5. (Color online) (a) Surface free energy γ, (b) first derivative γ', and (c) second derivative γ'' versus nanofilm thickness H from Eq. (17). Dashed black horizontal line in (a) corresponds to bulk film surface free energy γ_{bf} and green dash-dotted vertical lines represent Q_n from Eq. (10).

$$w_{\text{bulk}} \equiv pZ = \frac{NZ}{D^2H} = \frac{k_F^3}{3\pi^2}, \tag{7}$$

where $p=N/(D^2H)$ is the number of atoms per unit volume and Z is the valence electron number, we can obtain the Fermi energy as

$$\epsilon_f(n,H) = E_F\left[\frac{4Q}{3n} + \frac{(n+1)(2n+1)}{24q^2}\right], \tag{8}$$

where n is the number of Fermi discs inside the Fermi sphere, $Q \equiv H/\lambda_F$, $q \equiv \eta/\lambda_F = Q + \frac{3}{8}$, and the bulk (Drude-Sommerfeld) Fermi energy

$$E_F = \frac{\hbar^2}{2m_e}k_F^2 = \frac{\hbar^2}{2m_e}\frac{4\pi^2}{\lambda_F^2}. \tag{9}$$

It is easily verified from Eq. (8) that when $H \to \infty$ (therefore $n \to \infty$), $\epsilon_f \to E_F$. By definition, Eq. (8) only applies when $\epsilon_n(H) \le \epsilon_f(n,H) \le \epsilon_{n+1}(H)$. Define the crossing point of $\epsilon_f(n,H)$ and $\epsilon_n(H)$ as H_n, one can show that the applicability of Eq. (8) is from H_n to H_{n+1}. As film thickness H increases *continuously*, n will increase *one by one*. $\epsilon_f(n,H)$ is a smooth function for $H_n < H < H_{n+1}$ but the first derivatives of $\epsilon_f(n-1,H)$ and $\epsilon_f(n,H)$ at $H=H_n$ for $n>1$ are unequal, and consequently a cusp appears at such switch point from $n-1$ to n. The cusp positions $H_n = Q_n\lambda_F$ can be shown to satisfy

$$64Q_n^3 + 48Q_n^2 + 9Q_n = 8n^3 - 6n^2 - 2n \tag{10}$$

by letting $\epsilon_f(n,H_n)$ equal $\epsilon_n(H_n)$ with the use of Eqs. (8) and (5).

Figure 2 shows the Fermi energy ϵ_f from Eq. (8) and eigenvalues $\epsilon_{n=1,2,3,\ldots}$ from Eq. (5) versus nanofilm thickness H. As analyzed above, there are cusps on the ϵ_f curve at $H=H_n$ and the curve of ϵ_n versus H coincides with the nth

TABLE III. Surface free energies γ_{bf} for bulk Ag, Au, Mg, Al, and Pb films.

	Ag	Au	Mg	Al	Pb
γ_{bf} (meV/Å^2)	32.164	32.291	53.949	144.389	95.935

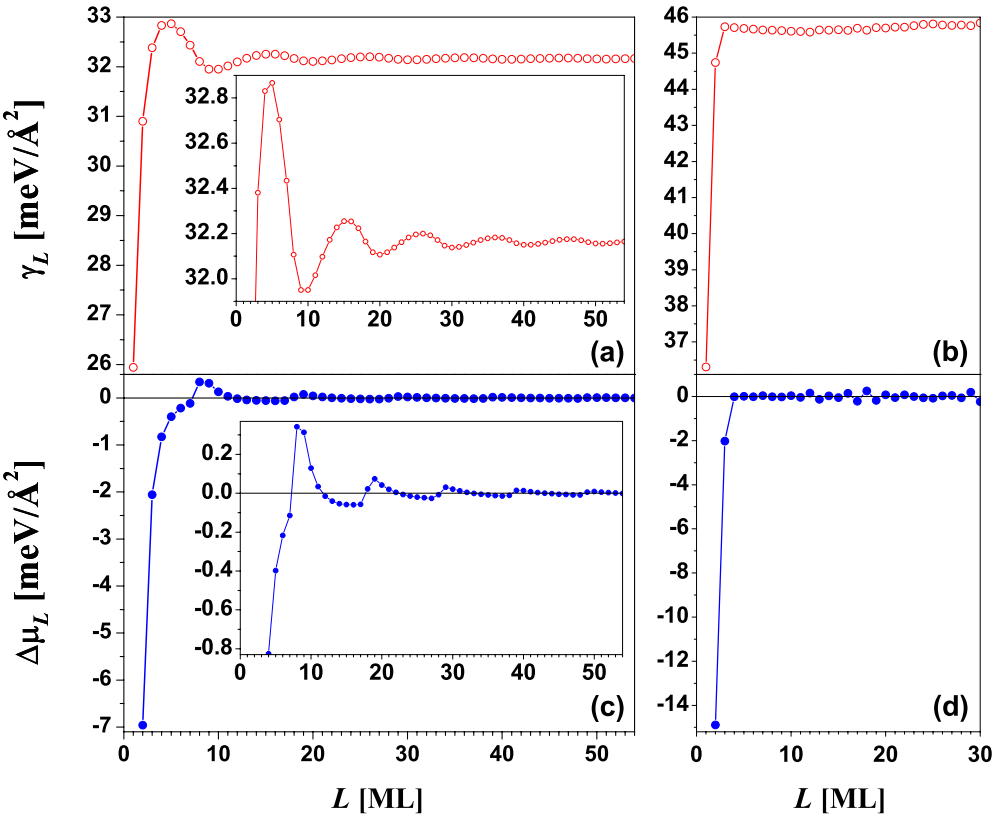

FIG. 6. (Color online) Surface free energy γ_L versus Ag(111) nanofilm thickness L from (a) EGM and (b) DFT calculations, respectively. Stability index $\Delta\mu_L$ versus L from (c) EGM and (d) DFT calculations, respectively. The insets in (a) and (c) provide expanded views.

cusp. With increasing H, the ϵ_f oscillates around the bulk Fermi energy E_F and the oscillation amplitude decreases gradually. Asymptotically, the upper envelope through the cusps can be approximately written as $E_F[1+1/(6n^2)]$ while the lower envelope through the local minima can be approximately written as $E_F[1-1/(12n^2)]$. For comparison, with $b=0$, ϵ_f versus H will deviate strongly from the result in Fig. 2 due to a spurious contribution $\propto 1/H$ [cf. Fig. 5(b) in Ref. 28].

To visualize more clearly the near periodicity of the oscillations in ϵ_f versus H in Fig. 2, from Eq. (10), we calculate the position H_n and the difference between neighboring cusps, as listed in Table II. With increasing H or n, the difference $H_{n+1}-H_n$ quickly approaches $\lambda_F/2$. From Eq. (10), the cusp position H_n can be expanded as

$$H_n = \frac{\lambda_F}{2}\left(n - \frac{3}{4} - \frac{1}{12n} - \frac{1}{24n^2} - \cdots\right). \tag{11}$$

The first two terms in the bracket correspond to the result from Schulte's free-electron-gas model analysis, in which a constant ϵ_f is assumed.[26] While an excellent approximation for large H or n, it deviates from the exact results significantly for small n. Nonetheless, the oscillatory behavior in ϵ_f with a near $\lambda_F/2$ periodicity is the same.

B. Ground-state electron density

The ground-state electron-density distribution can be calculated from

$$w(x,y,z) = \sum_{k_x,k_y,l} \psi^*_{k_x,k_y,l}(x,y,z)\,\psi_{k_x,k_y,l}(x,y,z), \tag{12}$$

where $\psi^*_{k_x,k_y,l}$ is the complex conjugate of $\psi_{k_x,k_y,l}$ and the summation runs over the NZ (total electron number in the supercell) lowest-lying occupied eigenstates (including spin). Substituting Eq. (3) into Eq. (12) and using the Fermi discs defined by Eq. (6), the electron density can be expressed as

$$w(z) = \frac{m_e}{\hbar^2\pi}\sum_{l=1}^{n}(\epsilon_f - \epsilon_l)\phi_n^2(z). \tag{13}$$

It is obvious that the electron density w is only the function of z for a jellium nanofilm with thickness H because of translational invariance in the xy plane. Note that the coordinate origin of z is at one hard-wall potential-well boundary (see Fig. 1) and the positive direction of z is toward the inside of the film. Thus, $w(z=b)$ gives the electron density at the geometric surface of the film, which is equivalent to $w(z=\eta-b)$, and $w(z=\eta/2)$ gives the electron density at the center of the film.

From Eqs. (13), (8), and (5), we obtain the ground-state electron density as

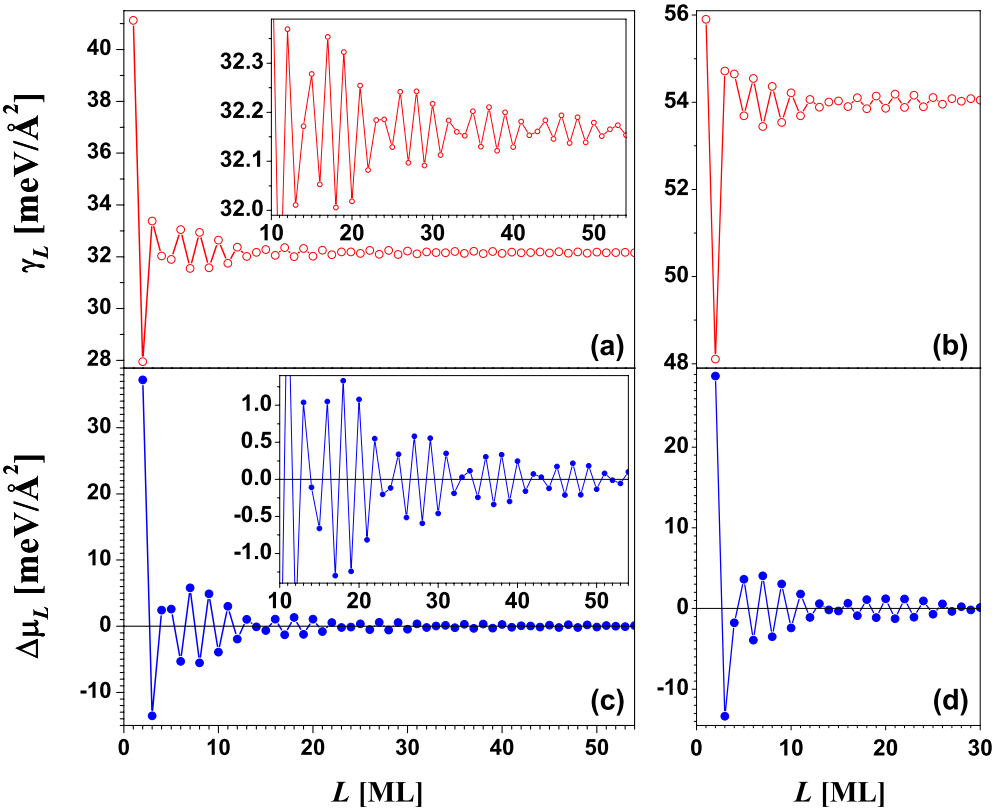

FIG. 7. (Color online) Surface free energy γ_L versus Ag(110) nanofilm thickness L from (a) EGM and (b) DFT calculations, respectively. Stability index $\Delta\mu_L$ versus L from (c) EGM and (d) DFT calculations, respectively. The insets in (a) and (c) are the corresponding local enlargements.

$$w(z) = \frac{w_{\text{bulk}}}{128nq^3}\{2(2n+1)(n^2+n+32Qq^2) + 6n(2n+1)\cot\xi\csc\xi\cos[(2n+1)\xi] + (8n^3+6n^2+n-64Qq^2-3n\cot^2\xi) \times\csc\xi\sin[(2n+1)\xi]-3n\csc^3\xi\sin[(2n+1)\xi]\}, \quad (14)$$

where $\xi \equiv z/\lambda_F$ and w_{bulk} is expressed by Eq. (7). In Eq. (14), the first term is independent of z and the other z-dependent terms give rise to the Bardeen-Friedel oscillations due to the existence of a surface,[41] as discussed below. It can be verified from Eq. (14) that when $H\to\infty$ (therefore $n\to\infty$), $w(z)$ approaches the well-known expression at bulk film limit.[37]

Figure 3 shows a three-dimensional (3D) oscillation surface of the electron density $w(z)$ versus H from Eq. (14). This 3D curve is analogous to Fig. 5 in Schulte's paper,[26] where the curve surface is obtained numerically from a self-consistent calculation of the jellium model. For any fixed thickness H, the electron density w oscillates as a function of position z due to the existence of a surface. For any fixed position z, the electron density w oscillates with cusps as a function of thickness H, and the positions of cusps are again determined by Eq. (10) with a period of $\sim\lambda_F/2$.

We illustrate the special case of the surface electron density $w(z=b)$ versus H, as shown in Fig. 4(a). From Fig. 4(a), it is clear that with increasing H, $w(b)$ steeply increases for extremely small H, and then oscillates with cusps and decreasing amplitudes around the value of κw_{bulk}, where the constant $\kappa=0.4557\ldots$. Another special case is the electron density at the center of the nanofilm $w(z=\eta/2)$ versus H, as shown in Fig. 4(b). From Fig. 4(b), $w(\eta/2)$ is also oscillatory as a function of H. With increasing H, $w(\eta/2)$ monotonically increases for any odd n and monotonically decreases for any even n.

C. Surface free energy

The surface free energy of a film is defined as

$$\gamma = \frac{E - NZ\sigma_{\text{bulk}}}{2A}, \quad (15)$$

where E is the total energy of supercell, NZ is the total electron number in the supercell, $A=D^2$ is the area of the bottom or top face of the supercell, and $\sigma_{\text{bulk}}=\frac{3}{5}E_F$ is the energy per electron for bulk metal from the Drude-Sommerfeld model.

By considering the Fermi discs defined by Eq. (6), it can be shown that the total energy of the film slab is

$$E = \frac{m_e D^2}{2\pi\hbar^2}\sum_{l=1}^{n}(\epsilon_f^2-\epsilon_l^2). \quad (16)$$

Substituting Eq. (16) into Eq. (15), and using Eqs. (8) and (5), we have

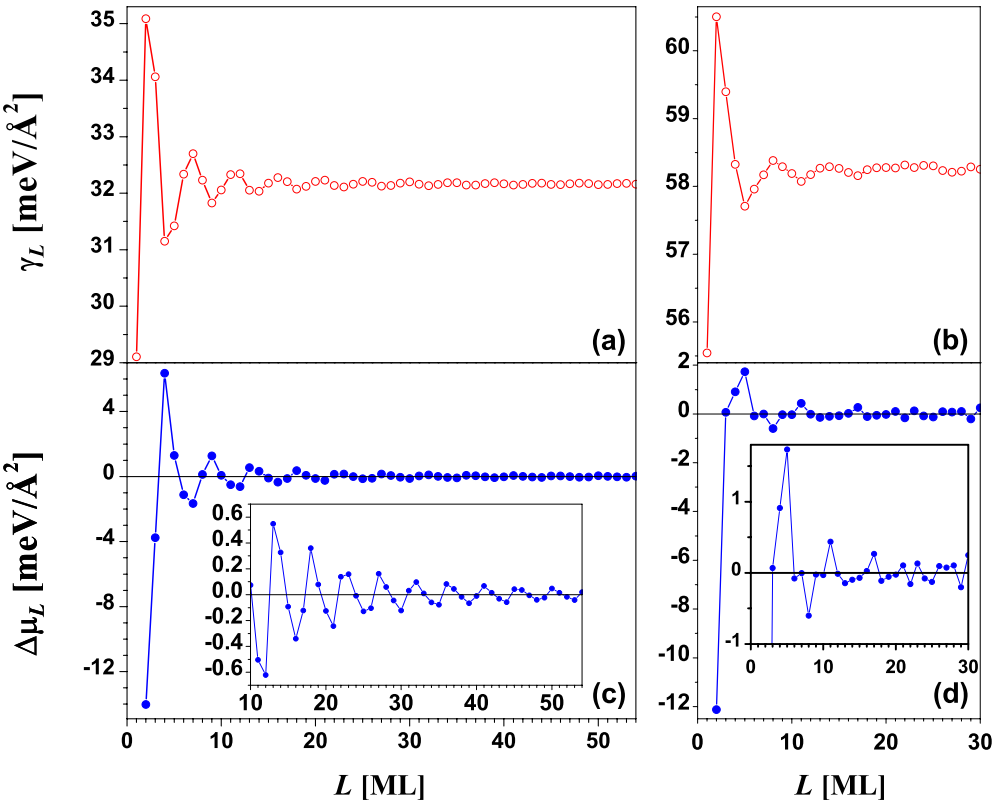

FIG. 8. (Color online) Surface free energy γ_L versus Ag(100) nanofilm thickness L from (a) EGM and (b) DFT calculations, respectively. Stability index $\Delta\mu_L$ versus L from (c) EGM and (d) DFT calculations, respectively. The insets in (c) and (d) are the corresponding local enlargements.

$$\gamma(n,H) = 10\gamma_{\rm bf}\left[\frac{16Q^2}{9n} + \frac{Q(n+1)(2n+1)}{9q^2} - \frac{n(n+1)(2n+1)(8n^2+3n-11)}{2880q^4} - \frac{8Q}{5}\right], \tag{17}$$

where the bulk film surface free energy $\gamma_{\rm bf}$ is expressed as

$$\gamma_{\rm bf} = \frac{\hbar^2}{2m_e}\frac{k_F^4}{80\pi} \tag{18}$$

as previously obtained by Huntington.[35] The values of $\gamma_{\rm bf}$ for five metals are listed in Table III. It is easily verified from Eq. (17) that when $H\to\infty$ (therefore $n\to\infty$), $\gamma\to\gamma_{\rm bf}$.

Equation (17) defines a family of *smooth* curves of $\gamma(n,H)$ versus H corresponding to different n but $\gamma(n,H)$ only determines the physical surface free energy for $H_n \le H \le H_{n+1}$. One can show that the γ curve thus obtained is C^1 continuous, i.e., at the switch point H_n for $n>1$, $\gamma(n-1,H)=\gamma(n,H)$, and $\gamma'(n-1,H)=\gamma'(n,H)$ but $\gamma''(n-1,H) \neq \gamma''(n,H)$, where γ' and γ'' denote the first and second derivatives of γ with respect to the dimensionless film thickness Q, respectively. Therefore, the switch points H_n for $n>1$ correspond to *inflection* points on the curve of γ versus H, as shown in Figs. 5(a)–5(c) [cf. Fig. 2, where the curve of ϵ_f versus H is C^0 continuous, i.e., $\epsilon_f(n-1,H)=\epsilon_f(n,H)$ but the first derivative is not continuous at H_n for $n>1$].

As shown in Fig. 5(a), γ versus H *resembles* a damped-sinusoidal function around the oscillation center $\gamma_{\rm bf}$ and the amplitude decays as $\sim 1/H^2$ asymptotically for large H. In contrast, for $b=0$, the oscillation of γ is not around $\gamma_{\rm bf}$ but asymptotically approaches the value of $5\gamma_{\rm bf}$. When $H=0$, the value of γ is infinity (see Fig. 6 in Ref. 28). Therefore, the behavior of γ versus H in ignoring charge spilling is remarkably different from Fig. 5(a) due to the spurious contribution $\propto 1/H$, as mentioned in Sec. I.

D. Comparison with previous models

Pitarke and Eguiluz also use an electron-gas model with the hard-wall potential, calling the model the infinite barrier model[27] to calculate surface free energy. The difference between their model and our electron-gas model is that they implicitly assume the Fermi energy ϵ_f to be a constant (i.e., the bulk value E_F). Therefore, they do not find oscillations as seen in Fig. 2. Then, they obtain a thickness-dependent z_0 (which is equivalent to our b) using the charge-neutrality requirement. As a result, the curve of surface free energy versus nanofilm thickness from their model is very different from Fig. 5(a). On their surface free-energy curve, there exist cusps which are always minima (see Fig. 4 in Ref. 27) while in Fig. 5(a) from our model, the corresponding points are always inflection points, as analyzed in Sec. II C. In other words, from our model, there exists a *phase shift* of $\sim\lambda_F/4$ between the maxima of the γ curve versus H and those of ϵ_f

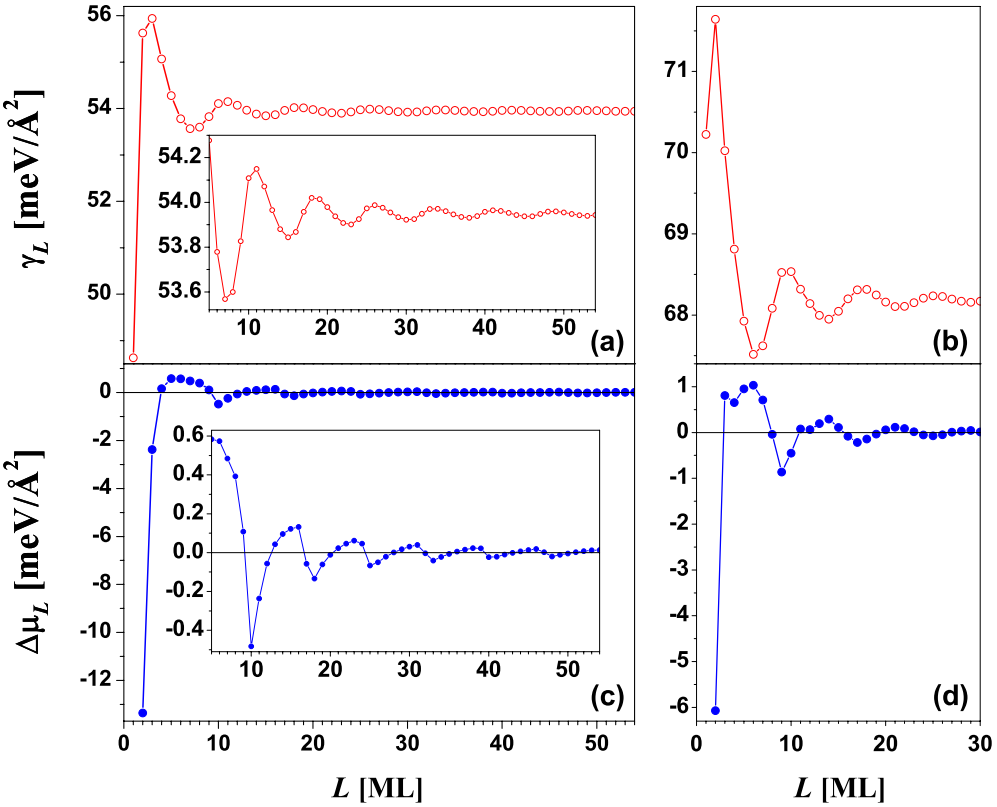

FIG. 9. (Color online) Surface free energy γ_L versus Mg(0001) nanofilm thickness L from (a) EGM and (b) DFT calculations, respectively. Stability index $\Delta\mu_L$ versus L from (c) EGM and (d) DFT calculations, respectively. The insets in (a) and (c) are the corresponding local enlargements.

curve versus H (cf. Figs. 5 and 2). The electron-density curves also differ between their model and ours. For example, in Fig. 4(b), there is always a cusp at any switch point from n to $n+1$ while in Fig. 2 of Ref. 27, there is a maximum instead of a cusp at the switch point from n to $n+1$ for any *odd* n.

Recently, Ogando *et al.*[42] determined the surface free energy versus the freestanding nanofilm thickness from a self-consistent calculation of the stabilized jellium model using the electron density of Pb. Our result, as shown in Fig. 5(a), is consistent with the "total" surface free-energy curve in Fig. 2(c) of Ref. 42, where indeed it is an inflection point but not a minimum at $H=H_n$, and the curve exhibits the damped-sinusoidal-like shape. This behavior is inconsistent with the result from Pitarke and Eguiluz's model in Ref. 27.

III. APPLICATIONS TO METAL NANOFILMS

For a metal electron-gas nanofilm, the thickness H is allowed to be continuous, as discussed in Sec. II. For a real metal nanofilm, the thickness H only takes the values of $H=Ld$, $L=1,2,3,\ldots$, i.e., the number of monolayers, L, can be used to label the thickness of the film. In order to compare with the results from DFT calculations or experiments for a real nanofilm, one should extract only the discrete values corresponding to $L=1,2,3,\ldots$ from the results obtained through the EGM. Below, to identify the discrete thickness, we add the subscript L to the symbol denoting the physical quantity, e.g., γ_L, E_L, etc., indicating the corresponding nanofilm thickness L in unit of ML.

To describe the thermodynamic stability of a real nanofilm, it is necessary to define a discrete second difference function, i.e., the "stability index"[20]

$$\Delta\mu_L = \frac{E_{L+1} + E_{L-1} - 2E_L}{A}, \tag{19}$$

where A is the area of the supercell base face. $\Delta\mu_L$ is related to chemical-potential-type quantities.[20,43,44] The physical interpretation of $\Delta\mu_L$ as follows: for $\Delta\mu_L<0$, a film with thickness L is unstable as it can lower its energy by bifurcating into films of thickness $L-1$ and $L+1$; for $\Delta\mu_L>0$, the film is stable against such a bifurcation.

Next, we analyze the oscillation period for a real nanofilm with the discrete thickness L. A simple useful rule can be obtained from Eq. (11) that if the interlayer spacing d is commensurate with an integer multiple of $\lambda_F/2$, i.e.,

$$jd \approx m\lambda_F/2, \tag{20}$$

where both $j>1$ and m are the smallest possible positive integers (with no common factor) then the film will display oscillatory behavior with a period of jd.

However, for a specific metal film, generally speaking, jd is never exactly equal to $m\lambda_F/2$, and this will result in a more complicated oscillatory pattern. In the simplest case, if

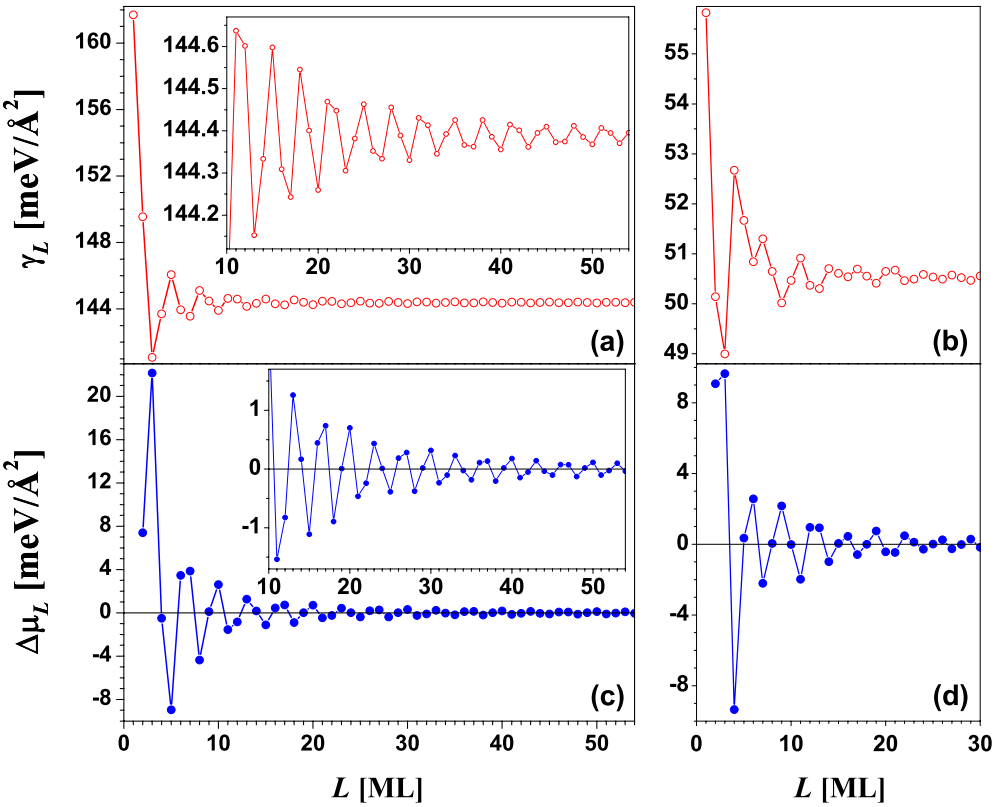

FIG. 10. (Color online) Surface free energy γ_L versus Al(111) nanofilm thickness L from (a) EGM and (b) DFT calculations, respectively. Stability index $\Delta\mu_L$ versus L from (c) EGM and (d) DFT calculations, respectively. The insets in (a) and (c) are the corresponding local enlargements.

$m\lambda_F/(2d)$ is sufficiently close but not exactly equal to the integer j then a beating pattern with a period of Λd occurs, where

$$\Lambda = \left| m - \frac{2jd}{\lambda_F} \right|^{-1}. \tag{21}$$

DFT calculations below for all metal films are performed using the plane-wave-based Vienna *ab initio* simulation package (VASP).[45] We use the PBE form of the generalized gradient approximation.[46] The interactions among electrons and ions are described by the projector augmented-wave approach.[47] In any DFT calculation in this work, we always relax all atoms in the supercell until the magnitude of the forces on all relaxed atoms is less than 0.01 eV/Å. The optimized lattice constants for bulk Ag, Mg, Al, and Pb are listed in Table I. These theoretical lattice constants were used in all subsequent calculations.

In Secs. III A–III J, we will show results for the surface free energies and stability indexes for Ag(111), Ag(110), Ag(100), Mg(0001), Al(111), Al(100), Al(110), Pb(111), Pb(100), and Pb(110) nanofilms, respectively. In all calculations of surface free energies, the surface size of periodic slab (supercell) is 1×1. The cutoff energies are always taken to be their VASP default values: 249.8, 210.0, 240.3, and 98.0 eV for Ag, Mg, Al, and Pb, respectively. To prevent spurious interactions between adjacent replicas of the thin-film system, we use a vacuum layer that is 15 Å thick in the direction perpendicular to the surface. We find that to achieve good convergence of surface energies, the number of **k** points taken for different metal films is very different. It will be individually specified in the following discussion. Also, because the surface free energy γ_L in Eq. (15) sensitively depends on the energy per atom, $E_c \equiv Z\sigma_{\text{bulk}}$, requiring stringent selection of the E_c value beyond the accuracy of DFT calculations, when calculating γ_L we always take E_c as an adjustable parameter with an uncertainty of roughly ±2 meV about the DFT value.[20]

A. Ag(111)

Figure 6 shows the QSE in the surface free energy and stability index for Ag(111) nanofilms from the EGM (left panels) and DFT calculations (right panels). The EGM results display an oscillatory pattern with a period of 10 ML. On the other hand, no significant oscillations can be detected from DFT calculations for $L>3$ ML. It should be mentioned that to obtain the well converged $\Delta\mu_L$ versus L from the DFT calculations, a very large **k**-point mesh is necessary and otherwise the significant numerical errors will appear, particularly for large L. In the DFT calculations of Figs. 6(b) and 6(d), the convergence is slow with increasing number of **k** points, and we take the **k**-point mesh to be $70\times70\times1$ (cf. our previous calculations[20]). From Figs. 6(b) and 6(d), there are no oscillations with the period of 10 ML. This is not consistent with Figs. 6(a) and 6(c). Nevertheless, the γ_L and

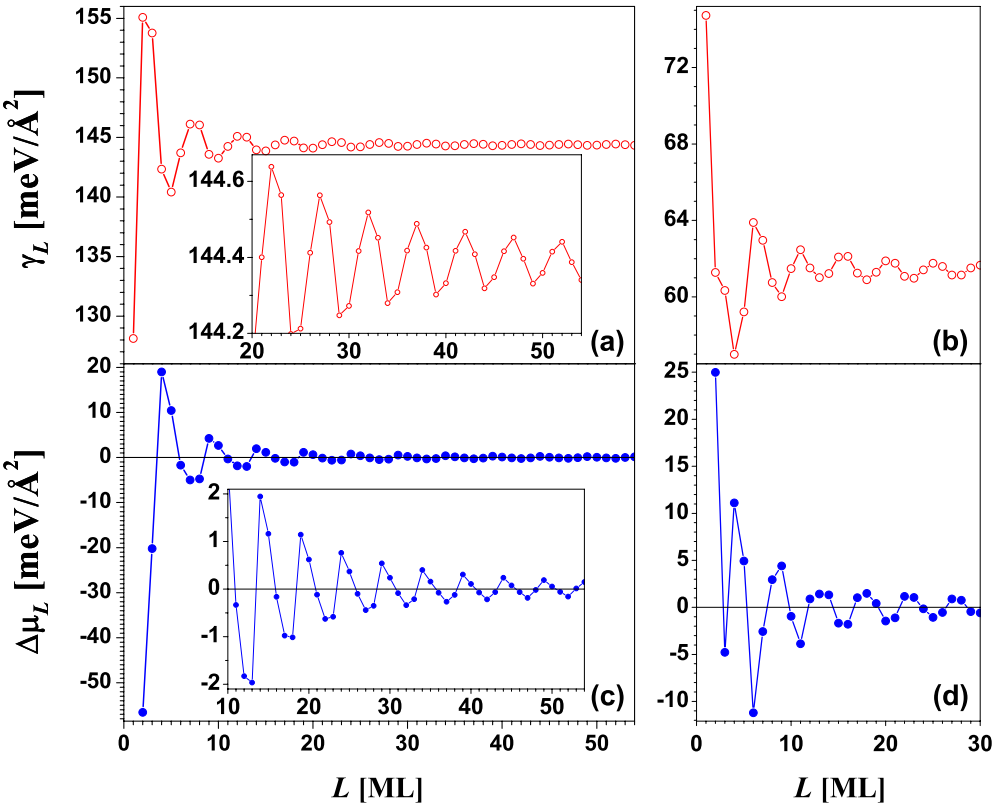

FIG. 11. (Color online) Surface free energy γ_L versus Al(110) nanofilm thickness L from (a) EGM and (b) DFT calculations, respectively. Stability index $\Delta\mu_L$ versus L from (c) EGM and (d) DFT calculations, respectively. The insets in (a) and (c) are the corresponding local enlargements.

$\Delta\mu_L$ curves exhibit overall consistency with the γ_L and $\Delta\mu_L$ curves in Figs. 6(b) and 6(d), respectively.

From Fig. 6(d), $\Delta\mu_L$ is approximately equal to zero when $L \geq 4$, indicating that Ag(111) films with different thicknesses have the almost same stability beyond the critical thickness $L_c=4$, i.e., Ag(111) nanofilms have the bulklike property for $L \geq 4$. Because $\Delta\mu_{L=2,3} < 0$, both $L=2$ and 3 are unstable. If there is a substrate surface underneath the Ag(111) film, the basic curve shape of $\Delta\mu_L$ versus L would not change, but the L_c value could have a "shift" depending on the property of the substrate material. The shift feature of γ_L, $\Delta\mu_L$, or other electronic properties versus L has been reported in the recent work for various systems.[12,13,20,48–50] It is then predicted that when Ag(111) nanofilms (or nanoislands with big enough lateral sizes) grow on a substrate surface in vacuum evaporation-deposition experiments with sufficient amounts of deposited Ag atoms, the Ag(111) islands with few layers should be unstable during the initial growth, and then the layer-by-layer growth mode dominates. This prediction is consistent with recent detailed experiments[51] for Ag deposition on Si(111)-7×7 surface, contrasting previous experiments[52,53] for this system.

B. Ag(110)

A Ag(110) nanofilm is a good example where both the primary oscillation and a beating pattern appear. For the Ag(110) film, $d=1.4386$ Å, $\lambda_F=5.2060$ Å, and $\lambda_F/(2d) = 1.8094 \approx 2$, so from Eq. (21), $\Lambda=9.49$. There should be a primary oscillation with the period of 2 ML and a beating pattern for the envelope of the primary oscillation with a period of 9.5 ML as shown in Figs. 7(a) and 7(c). For the Ag(110) nanofilm, the surface free energy γ_L [Fig. 7(a)] and stability index $\Delta\mu_L$ [Fig. 7(c)] versus L obtained from the EGM calculations are in good qualitative agreement with the corresponding results [Figs. 7(b) and 7(d)] from DFT calculations.

In the recent vacuum evaporation-deposition experiments for Ag on NiAl(110) surface,[13] an initial bilayer-by-bilayer growth mode of the Ag(110) nanofilm (or nanoislands) has been observed, consistent with the above analysis of two-layer oscillation. However, when the deposition coverage is higher ($L \gtrsim 6$ ML), the film structure will transform from Ag(110) towards Ag(111) (noting that the latter has a lower surface free energy than other crystalline planes of Ag). Thus, the beating effect cannot be easily accessed in these experiments. In addition, we also have shown that the NiAl(110) substrate induces a "phase shift" effect on the oscillation behavior while maintaining the basic oscillation features.[20] For more analysis details about the stability of Ag(110) films, see our recent work.[20]

In the DFT calculations, our tests show that $\Delta\mu_L$ versus L for a Ag(110) film converges faster with increasing **k** points than that for Ag(111) film [Figs. 6(b) and 6(d)]. In the DFT calculations of Figs. 7(b) and 7(d), the **k**-point mesh is $52\times52\times1$ (cf. Fig. 1 in Ref. 20, whereas the **k**-point mesh is $20\times20\times1$).

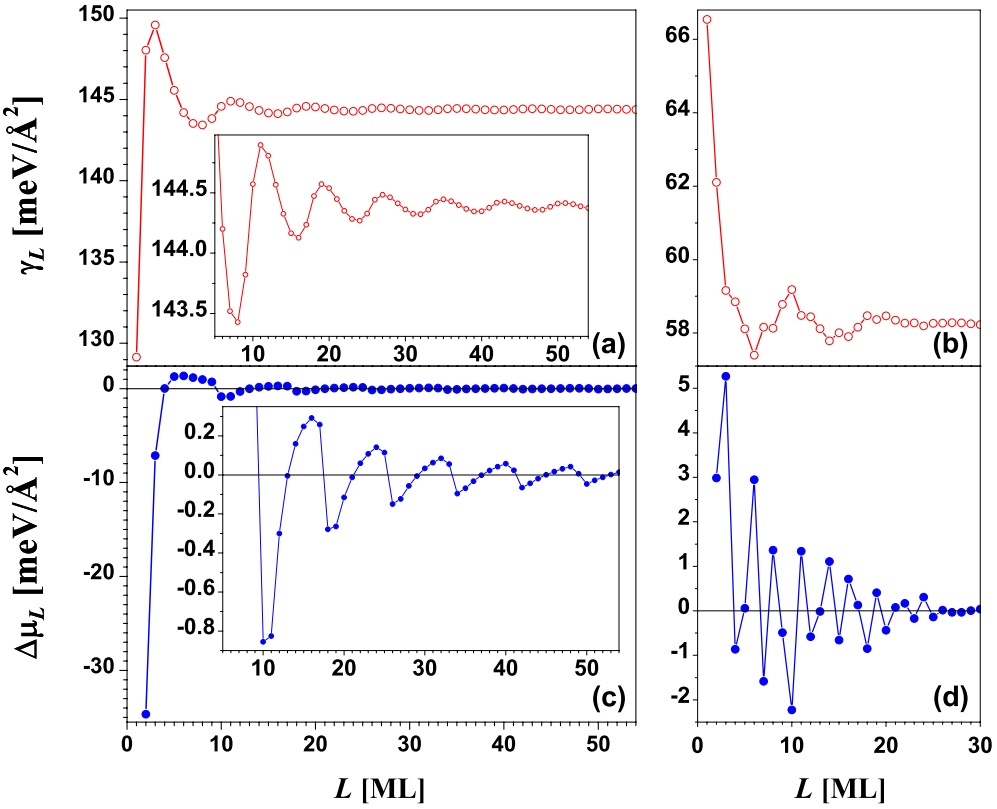

FIG. 12. (Color online) Surface free energy γ_L versus Al(100) nanofilm thickness L from (a) EGM and (b) DFT calculations, respectively. Stability index $\Delta\mu_L$ versus L from (c) EGM and (d) DFT calculations, respectively. The insets in (a) and (c) are the corresponding local enlargements.

C. Ag(100)

For a Ag(100) nanofilm, the EGM predicts a near 5 ML oscillatory behavior in γ_L and $\Delta\mu_L$, as shown in Figs. 8(a) and 8(c), respectively. This is in overall agreement with the corresponding results [Figs. 8(b) and 8(d)] from DFT calculations. In vacuum evaporation-deposition experiments for Ag on Fe(100) surface,[11,24] the growth mode of Ag(100) film is basically consistent with the above analysis that the oscillation period is about 4 or 5 ML. This is also confirmed from previous DFT calculations of Wei and Chou.[54] Similar behavior was observed in a theoretical DFT analysis for the growth of Ag(100) films on both Al- and Ni-terminated NiAl(100).[20]

Based on a series of convergence tests for $\Delta\mu_L$ versus L, a **k**-point mesh of $52\times52\times1$ suffices, and used in the DFT calculations of Figs. 8(b) and 8(d) (cf. Fig. 5 in Ref. 20, where the **k** mesh is $20\times20\times1$, which is not sufficiently large especially for the larger L).

D. Mg(0001)

Results for Mg(0001) nanofilms are shown in Fig. 9. The behavior of γ_L [Fig. 9(a)] and $\Delta\mu_L$ [Fig. 9(c)] versus L from the EGM calculations are in good agreement with the corresponding results [Figs. 9(b) and 9(d)] from DFT calculations, both exhibiting a 7–8 ML oscillation period. For additional discussion of this oscillation behavior, also see the early work of Feibelman[55] as well as the recent work of Li *et al.*[56] It should be pointed out that Fig. 3 for the surface free-energy analysis in the paper of Li *et al.*[56] fails to show clearly the above-mentioned oscillation period of ~7 or 8 ML. Most likely, this reflects the use of a too small **k**-point mesh of $11\times11\times1$. Based on a series of convergence tests on the curve of $\Delta\mu_L$ versus L, we use the **k**-point mesh of $61\times61\times1$ in our DFT calculations of Figs. 9(b) and 9(d).

E. Al(111)

Results for Al(111) are shown in Fig. 10. The behavior of γ_L [Fig. 10(a)] and $\Delta\mu_L$ [Fig. 10(c)] versus L from the EGM calculations is in overall agreement with the corresponding results [Figs. 10(b) and 10(d)] from DFT calculations. An oscillatory pattern with a period of 3–4 ML can be discerned. For additional discussion of this oscillation behavior, see the early work of Feibelman *et al.*[55,57] and the later work of Boettger.[58] It should be pointed out that the surface free-energy analysis in Fig. 3 in the paper by Boettger[58] fails to show the above-predicted oscillation period of ~3 or 4 ML. Most likely, this reflects the use of a too small **k**-point mesh even though it was $37\times37\times1$. Based on a series of convergence tests for $\Delta\mu_L$ versus L, we use a **k**-point mesh of $45\times45\times1$ in the DFT calculations of Figs. 10(b) and 10(d).

F. Al(110)

Results for Ag(110) are shown in Fig. 11. The behavior of γ_L [Fig. 11(a)] and $\Delta\mu_L$ [Fig. 11(c)] versus L from the EGM

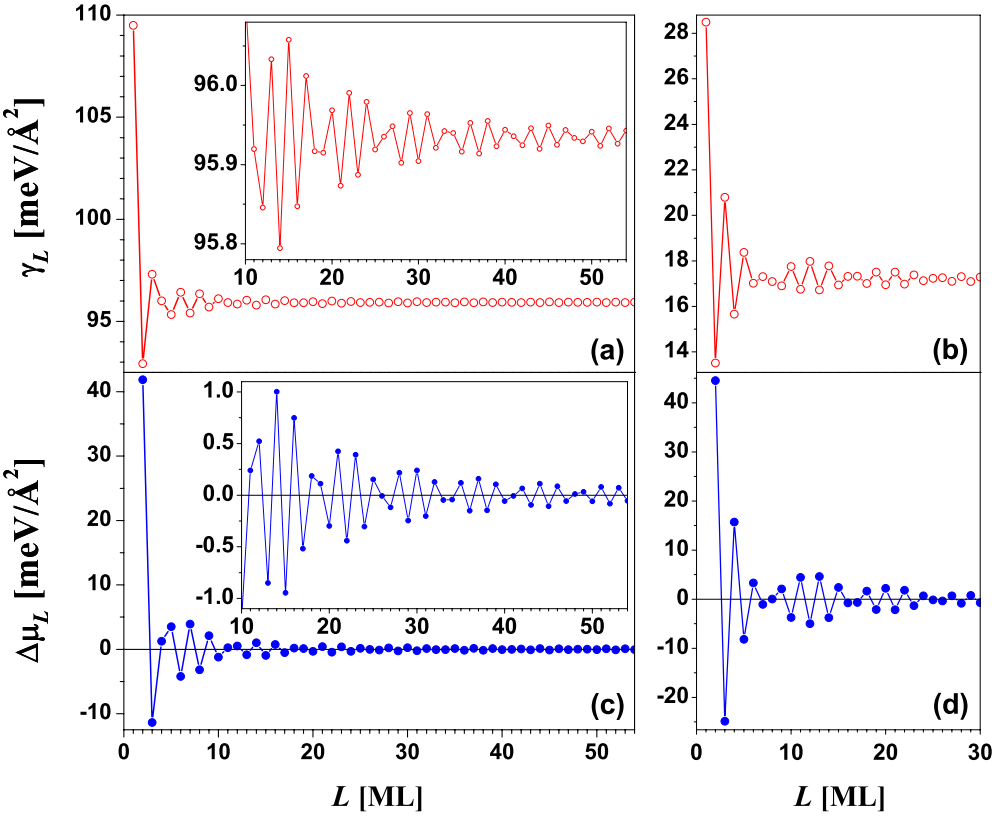

FIG. 13. (Color online) Surface free energy γ_L versus Pb(111) nanofilm thickness L from (a) EGM and (b) DFT calculations, respectively. Stability index $\Delta\mu_L$ versus L from (c) EGM and (d) DFT calculations, respectively. The insets in (a) and (c) are the corresponding local enlargements.

calculations is in overall agreement with the corresponding results [Figs. 11(b) and 11(d)] from DFT calculations, especially for the oscillation period of ~4 or 5 ML. However, the curve shapes from the EGM and DFT calculations have some noticeable difference, e.g., for small L, the trends of curves in Figs. 11(a) and 11(c) are the opposite of those in Figs. 11(b) and 11(d). We will discuss this inconsistency further in Sec. IV.

Based on a series of convergence tests for $\Delta\mu_L$ versus L, we use a **k**-point mesh of $46\times46\times1$ in the DFT calculations of Figs. 11(b) and 11(d). For the oscillation behavior of Al(110) film with increasing thickness, also see the work of Kiejna *et al.*[59] They used a DFT-based different method from us but obtained surface free-energy curve for L from 1 to 16 ML close to that in Fig. 11(b).

G. Al(100)

Results for Al(100) are shown in Fig. 12. The behavior of γ_L [Fig. 12(a)] and $\Delta\mu_L$ [Fig. 12(c)] versus L from the EGM calculations disagrees with the corresponding results [Figs. 12(b) and 12(d)] from DFT calculations, especially for the curve of $\Delta\mu_L$ versus L. The oscillation period is 7–8 ML for the EGM results, and 2–3 ML for the DFT results. This inconsistency will be discussed in Sec. IV. Based on a series of convergence tests for $\Delta\mu_L$ versus L, we use the **k**-point mesh of $71\times71\times1$ in the DFT calculations of Figs. 12(b) and 12(d).

H. Pb(111)

The QSE in Pb(111) nanofilms has been studied extensively both theoretically and experimentally.[60] Note that the Pb(111) surface has a lower surface free energy than other crystalline planes of Pb (Ref. 61) and therefore the Pb(111) film can be readily formed in experiments. However, most significantly, the amplitudes of both the first- and second-order oscillations are large enough and damp slowly with increasing Pb(111) nanofilm thickness so that the primary oscillation behavior with a "beating" pattern can be observed experimentally.

Results for Pb(111) are shown in Fig. 13. The behavior of γ_L [Fig. 13(a)] and $\Delta\mu_L$ [Fig. 13(c)] versus L from the EGM calculations is in good agreement with the corresponding results [Figs. 13(b) and 13(d)] from DFT calculations, showing bilayer oscillation with a beating pattern (with a period of 7.4 ML for EGM and around 9 ML for DFT). The analysis here for Pb(111) nanofilm is also consistent with the existing experimental results.[60] In the DFT calculations of Figs. 13(b) and 13(d), we use a **k** mesh of $60\times60\times1$.

Ayuela *et al.*[62] have recently performed the DFT calculations for Pb(111) films from $L=1$ to 60 ML and claim that the nonspherical Fermi surface due to two nesting Fermi wave vectors along the Pb[111] direction causes unusual beating pattern above 30 ML. The stability index curve from their DFT calculations for the first 30 ML is similar to Fig. 13(d). However, for $L\gtrsim30$ ML, we find from our tests that

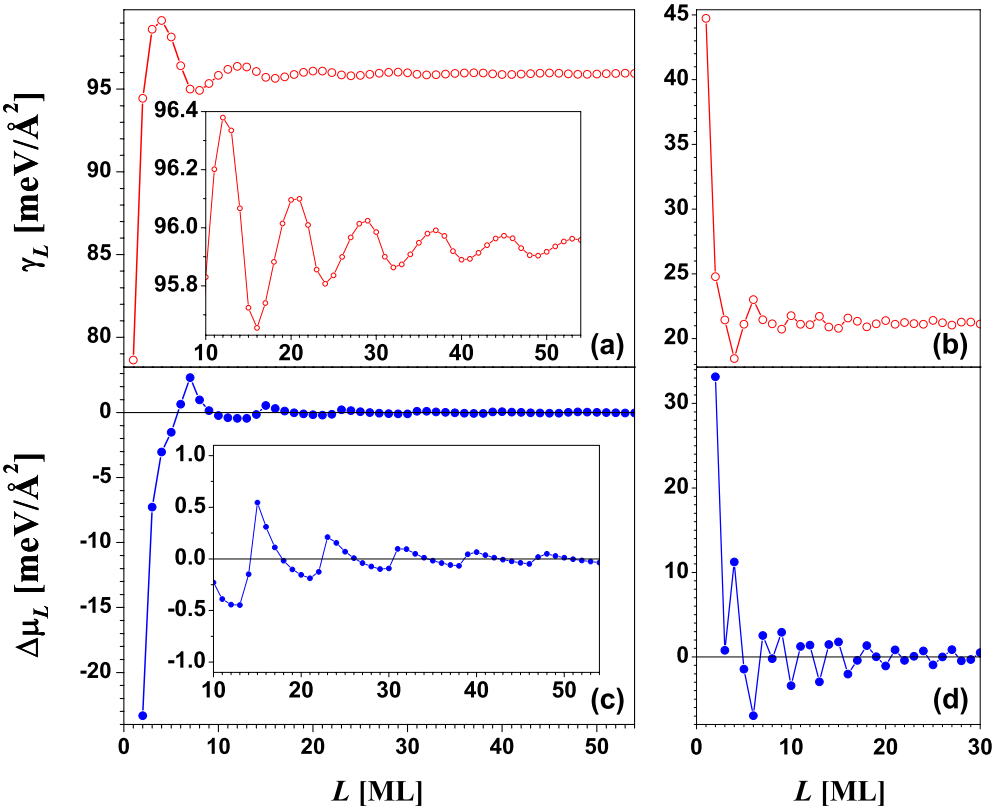

FIG. 14. (Color online) Surface free energy γ_L versus Pb(110) nanofilm thickness L from (a) EGM and (b) DFT calculations, respectively. Stability index $\Delta\mu_L$ versus L from (c) EGM and (d) DFT calculations, respectively. The insets in (a) and (c) are the corresponding local enlargements.

the shape of the curve is sensitive to the choice of the number of **k** points and the precision of DFT calculations beyond ~30 ML is insufficient to make a quantitative analysis for the effect of the Fermi-surface shape.

In the paper of Özer *et al.*,[63] the "electrons-in-a-box" model that they use does not yield apparent oscillations in the surface free energy. Even though they use a more realistic (corrugated background) potential, the surface free energy versus thickness L still displays a large discrepancy from the DFT results, especially for small L, where there clearly exists a spurious term $\propto 1/L$. The most likely reason is the absence of the charge spilling in their model, as already discussed in Secs. I and II.

I. Pb(110)

Results for Pb(110) are shown in Fig. 14. The behavior of γ_L [Fig. 14(a)] and $\Delta\mu_L$ [Fig. 14(c)] versus L from the EGM calculations is in major disagreement with the corresponding results [Figs. 14(b) and 14(d)] from DFT calculations. The oscillation period from the EGM is 8–9 ML while for DFT it is from 3 to 4 ML. A possible explanation is given in Sec. IV. Based on a series of convergence tests for $\Delta\mu_L$ versus L, we use the **k**-point mesh of $41\times41\times1$ in the DFT calculations of Figs. 14(b) and 14(d).

J. Pb(100)

Results for Pb(100) are shown in Fig. 15. The behavior of γ_L [Fig. 15(a)] and $\Delta\mu_L$ [Fig. 15(c)] versus L from the EGM calculations is in major disagreement with the corresponding results [Figs. 15(b) and 15(d)] from DFT calculations. The oscillation period is 4 ML for the EGM results while from DFT, the period is 2 ML. The likely reason is that the underlying lattice in Pb(100) nanofilms affects the band structures and the dispersion relationship. See Refs. 64 and 65 for more discussions. Based on a series of convergence tests on the curve of $\Delta\mu_L$ versus L, we use the **k**-point mesh of $41\times41\times1$ in the DFT calculations of Figs. 15(b) and 15(d).

IV. LIMITATIONS OF THE MODEL

It should be emphasized that the EGM with the hard-wall potential in this work constitutes an extreme simplification for realistic metal nanofilms. It cannot possibly describe accurately all physical properties of actual metal nanofilm although in some respects it is remarkably successful. Some improvements of the model can be pursued (while still maintaining the noninteracting feature): (i) because the potential-well barrier in our EGM is infinite, the model cannot be used to describe work function directly. To investigate the QSE of the work function as a function of nanofilm thickness, perhaps the simplest strategy is to choose the potential-well barrier U_0 to be a finite constant, and simultaneously adjust the charge spilling distance b to a suitable value. (ii) The EGM value of $\gamma_{L\to\infty}$ (also see Table III) only depends on the charge density and thus is independent of film orientation. This de-

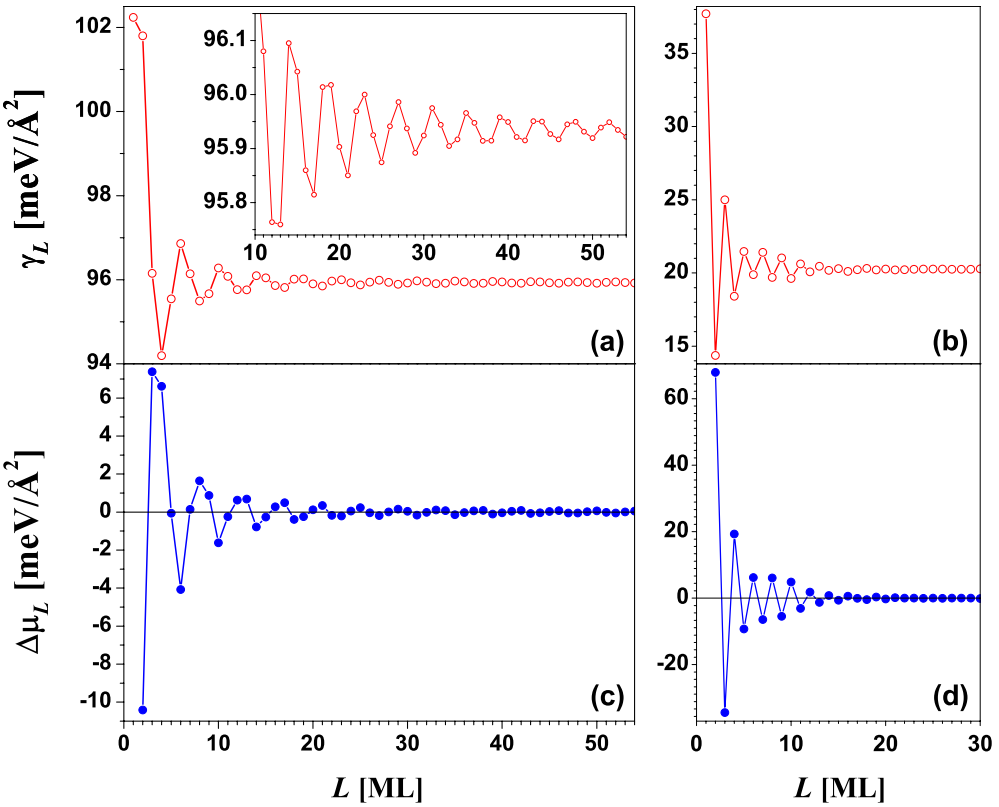

FIG. 15. (Color online) Surface free energy γ_L versus Pb(100) nanofilm thickness L from (a) EGM and (b) DFT calculations, respectively. Stability index $\Delta\mu_L$ versus L from (c) EGM and (d) DFT calculations, respectively. The inset in (a) is the corresponding local enlargement.

fect can be somewhat remedied by taking the interactions among ions and electrons into account.[66]

As pointed out in Sec. III, the oscillation behaviors obtained from the EGM for ten typical metal nanofilms are in varying degrees of consistency/inconsistency with the corresponding results from DFT calculations. In particular, for Al(100), Pb(110), and Pb(100) nanofilms, the oscillation curves and periods from the EGM are markedly different from the DFT results. The comparison between the EGM results and self-consistent jellium results shows very good overall agreements and the main reason for any discrepancy is related to the lattice distribution of the positive charges in a realistic metal crystal. This means that there are different potential distributions for different crystalline orientations, instead of simply taking constant U_0 or other isotropic (i.e., rotation-invariant) potentials. This results in an anisotropic and nonparabolic dispersion relationship.

Observations from nearly free-electron models of transition metals suggest that for 1-valence fcc(100), 1-valence fcc(110), and 2-valence hcp(0001) metal nanofilms, the anisotropic effect would be weak, and good agreement with the EGM should be expected. However, along the [111] direction, the Fermi surface of a noble metal lies above the free-electron-like s band[30] so that no crossings of the Fermi level and QWS occur with increasing nanofilm thickness. This is a likely reason why compared with the EGM, the DFT calculations show no noticeable regular oscillations for Ag(111) nanofilms [Figs. 6(b) and 6(d)] when the film thickness is bigger than 3 ML. For 3-valence Al(110) and Al(100) nanofilms, the anisotropic effect would be non negligible; for 4-valence Pb(110) and Pb(100), the anisotropic effect would be strong. For the bilayer oscillation behavior of Pb(100) nanofilm [see Figs. 15(b) and 15(d)], Yu *et al.*[64] as well as Wei *et al.*[65] provide some relevant energy-band analyses.

In addition, some other physical features such as the effect of the supporting substrate, the nanostructure geometry, etc., will also influence the results. In spite of these limitations, the model can satisfactorily reveal the basic oscillation behavior in electronic properties of metal nanofilms, indicating that the other factors beyond the noninteracting electron gas have relatively small contributions to the quantum-size features.

V. CONCLUSION

Noninteracting electron-gas "particle-in-a-box" models have been invoked frequently to describe the QSE in metal thin films. While the period and even the beating pattern can be readily obtained from any such model, the phase and magnitude are sensitive to the detailed construction of the model. In this paper, an EGM with an infinite potential barrier and a suitable treatment of charge spilling satisfactorily reveals the oscillation behavior of various electronic properties (such as Fermi energy, electron density, surface free energy, energy per electron, and dipole layer moment) versus metal nanofilm thickness, manifesting the regular relationship between the oscillation period and the Fermi wavelength. Comparison with published self-consistent jellium

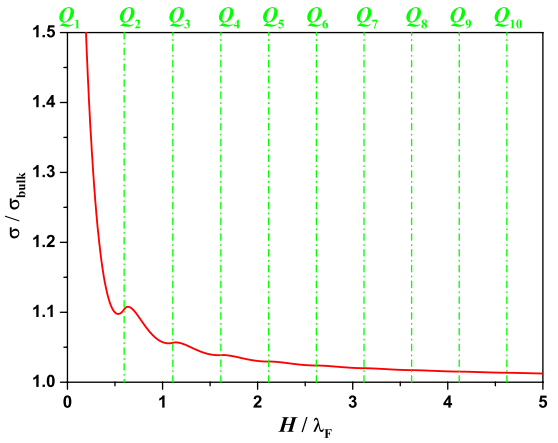

FIG. 16. (Color online) Energy per electron, σ, versus nanofilm thickness H from Eq. (A1). Green dash-dotted vertical lines represent Q_n from Eq. (10).

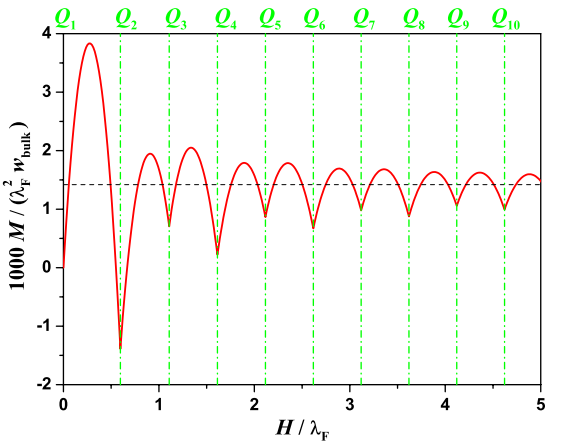

FIG. 17. (Color online) Dipole layer moment M versus nanofilm thickness H from Eq. (B4). Dashed black horizontal line corresponds to bulk film dipole layer moment $M_{\rm bf}$ and green dash-dotted vertical lines represent the cusps position Q_n from Eq. (10).

model results and our DFT results suggests that this model is superior to previous systematic studies of QSE using the electron-gas models with different simplifications regarding charge spilling.

By analyzing ten typical metal films and comparing with the results from DFT calculations, the overall quantum-size features of metal nanofilms are mainly attributed to the contribution from the confinement to noninteracting electron gas rather than the interaction effects of electrons and/or ion cores. For Ag(110), Ag(100), Mg(0001), Al(111), Al(110), and Pb(111) films, the oscillation features obtained from the EGM are in good or overall agreement with those from DFT calculations. However, for Al(100), Pb(110), and Pb(100) films, the oscillation behaviors from the model are markedly different with the results from DFT calculations. For Ag(111), the oscillatory feature of QSE is minimal.

After this manuscript was prepared, we noted a recently published paper[67] arriving at the same conclusion as our paper regarding the inflection points of the surface energy using a similar electron-gas model.

ACKNOWLEDGMENTS

Y.H. was supported for this work by NSF under Grant No. CHE-0809472. D.J.L. was supported by the Division of Chemical Sciences, Basic Energy Sciences, U.S. Department of Energy (U.S. DOE). Computational support at NERSC was provided by the U.S. DOE. We acknowledge a critical reading of the manuscript by James Evans. The work was performed at Ames Laboratory which is operated for the U.S. DOE by Iowa State University under Contract No. DE-AC02-07CH11358.

APPENDIX A: ENERGY PER ELECTRON

Substituting Eqs. (8) and (5) into Eq. (16), and dividing by total electron number $D^2Hw_{\rm bulk}$ [see Eq. (7) for $w_{\rm bulk}$], we obtain the energy per electron as

$$\sigma = \sigma_{\rm bulk}\left[\frac{10Q}{9n} + \frac{5(n+1)(2n+1)}{72q^2} - \frac{n(n+1)(2n+1)(8n^2+3n-11)}{4608Qq^4}\right], \tag{A1}$$

where $\sigma_{\rm bulk}=\frac{3}{5}E_F$ is the energy per electron for bulk metal from the Drude-Sommerfeld model. It is readily verified from Eq. (A1) that when $H\to\infty$ (therefore $n\to\infty$), $\sigma \to \sigma_{\rm bulk}$.

Figure 16 shows the form of σ versus H which exhibits steep oscillatory decay with increasing H to $\sigma_{\rm bulk}$. Ignoring charge spilling results in no noticeable oscillation [see Fig. 5(c) in Ref. 28]. Details of the analysis for σ versus H are similar to those for γ versus H in Sec. II C and are not presented here.

APPENDIX B: DIPOLE LAYER MOMENT

As shown in Fig. 3, around the region near the geometric surface of the jellium nanofilm, there is the significant charge spilling of electrons relative to the step-function positive charge background. Therefore, this will result in the formation of an electrostatic dipole layer. Thus, we define the dipole layer moment as

$$M = \int_0^{b+H/2} z(n_+ - n_-)dz. \tag{B1}$$

The negative charge density $n_-=w(z)$ and the positive charge density

$$n_+ = \begin{cases} 0 & \text{for } 0<z<b \\ w_{\rm bulk} & \text{for } b<z<b+\dfrac{H}{2}. \end{cases} \tag{B2}$$

Then, the dipole layer moment

$$M = -\int_0^b zw(z)dz + \int_b^{b+H/2} z[w_{\text{bulk}} - w(z)]dz \quad \text{(B3)}$$

or

$$\frac{M}{\lambda_F^2 w_{\text{bulk}}} = -\int_0^{3/16} \xi \frac{w(\xi)}{w_{\text{bulk}}} d\xi + \int_{3/16}^{3/16+Q/2} \xi \left[1 - \frac{w(\xi)}{w_{\text{bulk}}}\right] d\xi, \quad \text{(B4)}$$

where $w(\xi)$ is expressed by Eq. (14).

The variation in M versus H is plotted in Fig. 17 and also exhibits oscillatory behavior with cusps. The positions of these cusps are determined by Eq. (10) and therefore the oscillation period for the curve of M versus H is the same as that of ϵ_f versus H in Fig. 2. However, there is a notable difference between even and odd periods. The M value at a cusp position of any even n is always larger than its two neighboring M values at the cusp positions of $n-1$ and $n+1$, and specially, around the cusp at Q_2, the value of M is negative, as shown in Fig. 17. For the bulk film, one can obtain the bulk film dipole layer moment $M_{\text{bf}} \approx 0.0014\lambda_F^2 w_{\text{bulk}}$, which is the oscillation center of M versus H in Fig. 17.

*octavian2009@gmail.com

[1] M. L. Cohen and W. D. Knight, Phys. Today **43** (12), 42 (1990).
[2] W. A. de Heer, Rev. Mod. Phys. **65**, 611 (1993).
[3] M. Brack, Rev. Mod. Phys. **65**, 677 (1993).
[4] T. P. Martin, Phys. Rep. **273**, 199 (1996).
[5] T.-C. Chiang, Surf. Sci. Rep. **39**, 181 (2000).
[6] S. G. Frauendorf and C. Guet, Annu. Rev. Nucl. Part. Sci. **51**, 219 (2001).
[7] M. Milun, P. Pervan, and D. P. Woodruff, Rep. Prog. Phys. **65**, 99 (2002).
[8] V. Lindberg and B. Hellsing, J. Phys.: Condens. Matter **17**, S1075 (2005).
[9] M. C. Tringides, M. Jałochowski, and E. Bauer, Phys. Today **60** (4), 50 (2007).
[10] Y. Han, Fron. Phys. China **3**, 436 (2008).
[11] D.-A. Luh, T. Miller, J. J. Paggel, M. Y. Chou, and T.-C. Chiang, Science **292**, 1131 (2001).
[12] M. H. Upton, C. M. Wei, M. Y. Chou, T. Miller, and T.-C. Chiang, Phys. Rev. Lett. **93**, 026802 (2004).
[13] B. Unal, F. Qin, Y. Han, D.-J. Liu, D. Jing, A. R. Layson, C. J. Jenks, J. W. Evans, and P. A. Thiel, Phys. Rev. B **76**, 195410 (2007).
[14] M. Jałochowski and E. Bauer, Phys. Rev. B **38**, 5272 (1988).
[15] Y. Guo, Y.-F. Zhang, X.-Y. Bao, T.-Z. Han, Z. Tang, L.-X. Zhang, W.-G. Zhu, E. G. Wang, Q. Niu, Z. Q. Qiu, Jin-Feng Jia, Zhong-Xian Zhao, and Qi-Kun Xue, Science **306**, 1915 (2004).
[16] X.-Y. Bao, Y.-F. Zhang, Y. Wang, J.-F. Jia, Q.-K. Xue, X. C. Xie, and Z.-X. Zhao, Phys. Rev. Lett. **95**, 247005 (2005).
[17] T.-Z. Han, G.-C. Dong, Q.-T. Shen, Y.-F. Zhang, J.-F. Jia, and Q.-K. Xue, Appl. Phys. Lett. **89**, 183109 (2006).
[18] Y.-F. Zhang, Z. Tang, T.-Z. Han, X.-C. Ma, J.-F. Jia, Q.-K. Xue, K. Xun, and S.-C. Wu, Appl. Phys. Lett. **90**, 093120 (2007).
[19] C. M. Wei and M. Y. Chou, Phys. Rev. B **66**, 233408 (2002).
[20] Y. Han, J. W. Evans, and D.-J. Liu, Surf. Sci. **602**, 2532 (2008).
[21] L.-Y. Ma, L. Tang, Z.-L. Guan, K. He, K. An, X.-C. Ma, J.-F. Jia, Q.-K. Xue, Y. Han, S. Huang, and Feng Liu, Phys. Rev. Lett. **97**, 266102 (2006).
[22] Y. Han, M. Hupalo, M. C. Tringides, and F. Liu, Surf. Sci. **602**, 62 (2008).
[23] Y. Han, B. Unal, F. Qin, D. Jing, C. J. Jenks, D.-J. Liu, P. A. Thiel, and J. W. Evans, Phys. Rev. Lett. **100**, 116105 (2008).
[24] J. J. Paggel, C. M. Wei, M. Y. Chou, D.-A. Luh, T. Miller, and T.-C. Chiang, Phys. Rev. B **66**, 233403 (2002).
[25] Y. Qi, X. Ma, P. Jiang, S. Ji, Y. Fu, J.-F. Jia, Q.-K. Xue, and S. B. Zhang, Appl. Phys. Lett. **90**, 013109 (2007).
[26] F. K. Schulte, Surf. Sci. **55**, 427 (1976).
[27] J. M. Pitarke and A. G. Eguiluz, Phys. Rev. B **63**, 045116 (2001).
[28] B. Wu and Z. Zhang, Phys. Rev. B **77**, 035410 (2008).
[29] J. Bardeen, Phys. Rev. **49**, 653 (1936).
[30] N. W. Ashcroft and N. D. Mermin, *Solid State Physics* (Saunders, Philadelphia, 1976).
[31] A. K. Giri and G. Mitra, J. Phys. D **18**, L75 (1985).
[32] D. Shoenberg, Philos. Trans. R. Soc. Lond. A **255**, 85 (1962).
[33] W. Joss, Phys. Rev. B **23**, 4913 (1981).
[34] W. B. Pearson, *A Handbook of Lattice Spacings and Structures of Metals and Alloys* (Pergamon, New York, 1958).
[35] H. B. Huntington, Phys. Rev. **81**, 1035 (1951).
[36] K. Huang and G. Wyllie, Proc. Phys. Soc. A **62**, 180 (1949).
[37] R. Stratton, Philos. Mag. **44**, 1236 (1953).
[38] B. G. Smith, Phys. Lett. **18**, 210 (1965).
[39] R. Stratton, Phys. Lett. **19**, 556 (1965).
[40] W. A. Atkinson and A. J. Slavin, Am. J. Phys. **76**, 1099 (2008).
[41] Viraht Sahni (private communication); also see Refs. 29 and 37, and Viraht Sahni, *Quantal Density Functional Theory II: Approximation Methods and Applications* (Springer-Verlag, Berlin, in press).
[42] E. Ogando, N. Zabala, E. V. Chulkov, and M. J. Puska, J. Phys.: Condens. Matter **20**, 315002 (2008).
[43] Y. Han, J. Y. Zhu, F. Liu, S.-C. Li, J.-F. Jia, Y.-F. Zhang, and Q.-K. Xue, Phys. Rev. Lett. **93**, 106102 (2004).
[44] Y. Han and F. Liu, Fron. Phys. China **3**, 41 (2008).
[45] G. Kresse and J. Hafner, Phys. Rev. B **47**, 558 (1993).
[46] J. P. Perdew, K. Burke, and M. Ernzerhof, Phys. Rev. Lett. **77**, 3865 (1996).
[47] G. Kresse and D. Joubert, Phys. Rev. B **59**, 1758 (1999).
[48] Y. Jia, B. Wu, H. H. Weitering, and Z. Zhang, Phys. Rev. B **74**, 035433 (2006).
[49] J. H. Dil, T. U. Kampen, B. Hülsen, T. Seyller, and K. Horn, Phys. Rev. B **75**, 161401(R) (2007).
[50] Y. Liu, J. J. Paggel, M. H. Upton, T. Miller, and T.-C. Chiang, Phys. Rev. B **78**, 235437 (2008).
[51] B. Ünal *et al.* (unpublished).
[52] L. Gavioli, K. R. Kimberlin, M. C. Tringides, J. F. Wendelken,

and Z. Zhang, Phys. Rev. Lett. **82**, 129 (1999).
[53] D. K. Goswami, K. Bhattacharjee, B. Satpati, S. Roy, P. V. Satyam, and B. N. Dev, Surf. Sci. **601**, 603 (2007).
[54] C. M. Wei and M. Y. Chou, Phys. Rev. B **68**, 125406 (2003).
[55] P. J. Feibelman, Phys. Rev. B **27**, 1991 (1983).
[56] X.-G. Li, P. Zhang, and C. K. Chan, Physica B (Amsterdam) **390**, 225 (2007).
[57] P. J. Feibelman and D. R. Hamann, Phys. Rev. B **29**, 6463 (1984).
[58] J. C. Boettger, Phys. Rev. B **53**, 13133 (1996).
[59] A. Kiejna, J. Peisert, and P. Scharoch, Surf. Sci. **432**, 54 (1999).
[60] See Refs. 2–24 cited in Ref. 20 for example.
[61] Y. Han, G.-H. Lu, B.-J. Lee, and F. Liu, Surf. Sci. **602**, 2284 (2008).
[62] A. Ayuela, E. Ogando, and N. Zabala, Phys. Rev. B **75**, 153403 (2007).
[63] M. M. Özer, Y. Jia, B. Wu, Z. Zhang, and H. H. Weitering, Phys. Rev. B **72**, 113409 (2005).
[64] D. Yu, M. Scheffler, and M. Persson, Phys. Rev. B **74**, 113401 (2006).
[65] C. M. Wei and M. Y. Chou, Phys. Rev. B **75**, 195417 (2007).
[66] N. D. Lang and W. Kohn, Phys. Rev. B **1**, 4555 (1970).
[67] T. Miller, M. Y. Chou, and T.-C. Chiang, Phys. Rev. Lett. **102**, 236803 (2009).